Food Research International 157 (2022) 111049

Contents lists available at ScienceDirect

Food Research International

journal homepage: www.elsevier.com/locate/foodres

Revealing how maltodextrin-containing droplets dry using optical coherence tomography

Erik J.G. Sewalt [a], J. Kalkman [b], J.R. van Ommen [a], Gabrie M.H. Meesters [a], V. van Steijn [a,*]

[a] Department of Chemical Engineering, Delft University of Technology, 2628 CJ Delft, the Netherlands
[b] Department of Imaging Physics, Delft University of Technology, 2628 CJ Delft, the Netherlands

ARTICLE INFO

Keywords:
Drying droplet
Optical coherence tomography
Component reorganization during drying
Particle morphology
Stickiness
Spray drying
Single droplet drying

ABSTRACT

Properties of powders produced from drying solute-containing droplets arise from the dynamic redistribution of solute during drying. While insights on the dynamic redistribution are instrumental for the rational design of powders and for the optimized operation of equipment such as spray dryers, experimental techniques that allow measuring the spatio-temporal concentration of solute in drying droplets are scarce. In this work, we explore and demonstrate the use of optical coherence tomography (OCT) to measure the spatio-temporal concentration of solute in drying droplets and the development of a solidifying shell at the liquid-air interface, using aqueous droplets of maltodextrin as a model system. This work provides a solid foundation for the use of OCT to quantify the dynamic redistribution of solute and link it to the development of the morphology of the produced particles and agglomerates.

1. Introduction

Production of powders from solute-containing microdroplets is fundamental to various processing technologies in the food and pharmaceutical sector (Santos et al., 2018). Bulk properties of powders, such as flowability and dispersibility, are dictated by the morphology of the produced agglomerates. Inspection of powders from processes such as spray drying shows that agglomerates consist of particles with a wide range of morphologies, including solid and hollow particles, with smooth, crumbled, or broken shells (Walton, 2000). The morphology of individual particles stems from the dynamic interplay between the evaporation of solvent from the droplets and the redistribution of solute such as carbohydrates, fibers, or proteins inside them (Sadek et al., 2015). Solute can continuously redistribute in the interior of slow-drying droplets by diffusion, leading to solid particles without shells. Conversely, solute accumulates at the surface of fast-drying droplets, leading to particles with shells that may buckle depending on their morphology and composition (Vehring, Foss, & Lechuga-Ballesteros, 2007; Bansal, Miglani, & Basu, 2015). The distribution of solute also governs the dynamic properties of the droplets' surfaces that can temporarily become sticky, which promotes the formation of agglomerates through collisions with other semi-wet particles (Sewalt, Zhang, van Steijn, van Ommen, & Meesters, 2020; van der Hoeven, 2008). A deep understanding of the dynamic redistribution of solute in drying droplets is instrumental for two main reasons: First, from a particle engineering perspective, it allows for the engineering of the final powder structure. Second, from a process engineering perspective, it helps to determine processing boundaries, enabling a more cost-efficient design of equipment such as spray dryers.

Experimental techniques to study the drying of solute-containing droplets allow immobilization of the droplet by deposition on a flat solid surface, levitation in air, or suspension from a needle. While brightfield imaging of such droplets elucidates the drying kinetics and morphological changes (Fu, Woo, & Chen, 2012; Sadek et al., 2015), measuring the dynamic redistribution of solute inside drying droplets presents a significant challenge (Schutyser, Both, Siemons, Vaessen, & Zhang, 2019). A fully dried particle's surface can be characterized ex situ with X-ray photoelectron spectroscopy (XPS) and confocal Raman spectroscopy, showing the influence of solute component properties on phase segregation (Nuzzo, Sloth, Brandner, Bergenstahl, & Millqvist-Fureby, 2015; Munoz-Ibanez et al., 2016; Nuzzo, Overgaard, Bergenståhl, & Millqvist-Fureby, 2017; Both, Nuzzo, Millqvist-Fureby, Boom, & Schutyser, 2018). Arresting the state of the droplet at different instants during the drying process by flash-freezing with liquid nitrogen provides a means to construct the dynamics through ex situ characterization of the chemical surface composition with XPS and the internal distribution

* Corresponding author.
E-mail addresses: e.j.g.sewalt@tudelft.nl (E.J.G. Sewalt), V.vanSteijn@tudelft.nl (V. van Steijn).

https://doi.org/10.1016/j.foodres.2022.111049
Received 17 September 2021; Received in revised form 24 January 2022; Accepted 18 February 2022
Available online 2 April 2022

with confocal microscopy (Foerster, Gengenbach, Woo, & Selomulya, 2016). Techniques for in situ probing the redistribution of solute in drying micro-droplets are scarce (Lemoine & Castanet, 2013; Schutyser et al., 2019; De Souza Lima, Ré, & Arlabosse, 2020). Examples include rainbow refractometry (Lemoine & Castanet, 2013), which becomes inaccurate upon introduction of gradients in the refractive index, nuclear magnetic resonance spectroscopy (Griffith, Bayly, & Johns, 2008), which is limited in spatial and temporal resolution, and Raman spectroscopy (Tuckermann, Puskar, Zavabeti, Sekine, & McNaughton, 2009; Quiño et al., 2015). Quiño et al., 2015 successfully used in situ Raman microscopy to measure the component distribution of a large acetone-water droplet ($d \approx 2$ mm) evaporating in an acoustic levitator. However, improving the resolution below 120 μm was difficult due to light distortion near the liquid-air interface (De Souza Lima et al., 2020). A promising in situ method is laser speckle imaging (LSI), as it can non-invasively probe inside turbid droplets at high spatial and temporal resolution. LSI was used to visualize colloid particle mobility and the 'coffee ring' effect in a drying paint droplet with a spatial resolution up to 5 μm (Van Der Kooij, Fokkink, Van Der Gucht, & Sprakel, 2016). Another promising technique, which has received limited attention for the application to drying droplets, and specifically for measuring the dynamic solute distribution, is optical coherence tomography (OCT) (Koponen & Haavisto, 2020). OCT was originally developed for the field of ophthalmology and is a non-intrusive imaging technique that allows characterization of opaque samples. It is based on a Michelson interferometer that uses the back-scattering of near-infrared light to image samples (Izatt, Choma, & Dhalla, 2015) The application to droplets has focused on visualization of internal flow patterns (Srinivasan et al., 2003; Manukyan et al., 2013; Edwards et al., 2018), visualization of phase changes (Davidson et al., 2017), monitoring of rehydration (Lee, Bathany, Ahn, Takayama, & Jung, 2016). In our view, OCT also has a high potential to in situ measure the dynamic distribution of solute and development of internal structures in evaporating droplets with micrometer resolution.

In this work, we explore the use of OCT for the in situ measurement of the dynamic distribution of solute during the drying of turbid solute-containing droplets. We use a sessile maltodextrin droplet as the model system, as maltodextrins are common in the food industry and their influence on dried particle morphology is well known (Both et al., 2018; Both, Siemons, Boom, & Schutyser, 2019; Siemons, Politiek, Boom, van der Sman, & Schutyser, 2020). We demonstrate that OCT can be used to measure the drying kinetics, the solute distribution, the formation of a shell, and the internal convective flows. We demonstrate a method to map the component concentration in a drying droplet by quantifying the diffusivity of tracer particles, which can be used to estimate the local viscosity, and hence maltodextrin concentration, with at least order-of-magnitude accuracy. This work provides a solid foundation for using OCT as a characterization method for drying droplets, where the insights could guide the design of powders with desired properties. Additionally, thus obtained data is crucial for the validation of theoretical/numerical models of droplet drying (Meerdink & van't Riet, 1995; Mezhericher, Levy, & Borde, 2010).

2. Materials and methods

2.1. Solution preparation

Maltodextrin with a dextrose equivalent of 12 (MD12, Glucidex) was mixed with deionized water to obtain a 10 wt% MD12 solution, which has a viscosity of 1.1 mPas (Both et al., 2019). A 10 wt% MD12 concentration was chosen to illustrate the possibilities of the OCT measurements, because drying of this solution does result in the formation of a detectable skin at the interface, while the viscosity remains sufficiently low throughout the drying process to characterize it with the chosen OCT settings. Contrast in the OCT measurements was enhanced by addition of 0.1 wt% titanium dioxide nanoparticles (TiO_2 P25 AEROXIDE). Individual TiO_2 nanoparticles have a diameter of 25 nm, but they form larger agglomerates. The size of the TiO_2 agglomerates was measured before the measurements, as explained later. We will refer to these agglomerates as TiO_2 particles throughout this paper. While the agglomeration affected their size, requiring calibration of the size in the solution, we found that the optical advantages of TiO_2 outweighed this disadvantage.

2.2. Substrate preparation

Sylgard 184 Poly(dimethylsiloxane) (PDMS) elastomer and curing agent were obtained for making a superhydrophobic substrate. PDMS was degassed, poured onto polishing sandpaper (30000 grains/cm^2, Airbrush, Almere), and subsequently cured at 70 °C overnight. Removal of the sandpaper resulted in a PDMS substrate with micro-roughness. The contact angle was determined optically from droplets of Milli-Q water deposited on top of the substrate. The resulting contact angle was 154 ± 4°.

2.3. Droplet drying experiment

Droplets were generated and ejected onto the superhydrophobic substrate using a PipeJet P9 NanoDispenser (BioFluidix GmbH, Freiburg) equipped with a nozzle having an orifice size of 500 μm. Using a stroke of 100% and a stroke velocity of 80 μm s^{-1}, we generated droplets with a volume of 42.2 nL, giving an equivalent spherical diameter of 432 μm. Immediately after droplet deposition on the substrate, the substrate was placed on a micro stage under the imaging head of the OCT system, with the imaging direction in the axial (z) direction, perpendicular to the substrate, see Fig. 1. The micro stage allowed for rapid and precise placement of the droplets. The approximate time between dispensing the droplet and the start of OCT imaging was 9 s. During imaging, droplets evaporated in ambient air with a temperature of 20 °C and a relative humidity of 35%. Their full evaporation took approximately 240 s.

2.4. Optical Coherence Tomography measurements

Measurements on the droplets were made with a high-resolution spectral-domain OCT system (Ganymede-II-HR, Thorlabs Inc., Germany). This system was equipped with a long working distance lens (OCT-LK4-BB lens, Thorlabs Inc., Germany) and used near-infrared light with a center wavelength of $\lambda_c = 900$ nm and a bandwidth of 195 nm

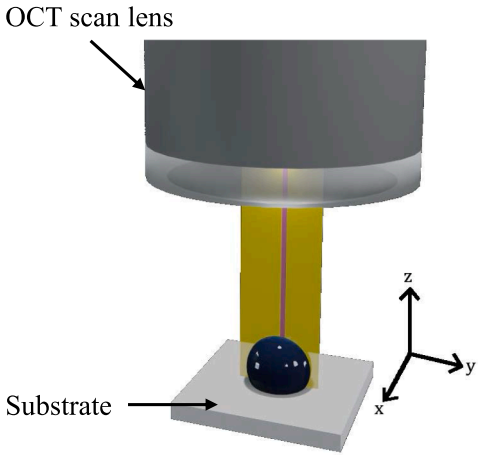

Fig. 1. Rendered image of the optical coherence tomography setup with a sessile maltodextrin (MD12) droplet. The yellow sheet indicates the orientation of the 2D scans. The magenta line indicates the orientation of the 1D scans. (For interpretation of the references to colour in this figure legend, the reader is referred to the web version of this article.)

(Callewaert, Dik, & Kalkman, 2017). It allowed imaging up to a depth of 1.89 mm, which is four times larger than the height of the droplets. By overlapping the focus point of the OCT sample arm with the droplet, the strength of the signal was maximized.

Two types of OCT measurements were performed on the drying droplets, a sequence of 1D scans performed at a fixed location showing the fast dynamics along a 1D line and a sequence of 1D scans taken while moving the OCT beam laterally, showing the slower dynamics in a 2D plane, see Fig. 1.

The dynamic redistribution of MD12 was measured by taking 1D (often referred to as A-scans in the OCT literature) scans near the apex of the droplets. Since interfaces that are perpendicular to the beam, i.e., the air-liquid interface at the droplets' apex, result in a high scattering intensity that can overload the sensor, we used a slight lateral offset to avoid overexposure. Using Fourier domain OCT, all sampling volumes in a single 1D scan, over the full depth of a droplet, were measured simultaneously, with the dimensions of the sampling volumes of 6.7 μm × 6.7 μm × 2.6 μm being dictated by the optical resolution in the lateral (x and y) and axial (z) direction. We note that the axial resolution is highest at the focus point and decreases slightly with increasing distance from the focus point. In all of our experiments, the axial sampling resolution was 1.95 μm, as this resolution is set by the spectral resolution of the OCT system. Temporal fluctuations arising from the scattering of light from TiO_2 particles moving through the individual sampling volumes were measured by taking 10000 consecutive A-scans at a single lateral location at a rate of 5.5 kHz for a total scan time of 1.82 s. From the resulting sequence of 1D scans (often referred to as an M-scan), the diffusion coefficient of the TiO_2 particles was determined, which in turn was converted to the concentration of MD12, as explained later. Consecutive M-scans were taken at intervals of 3.65 s (0.27 Hz) during the drying period of 240 s. Hereafter, we will colloquially refer to M-scans as '1D OCT' scans.

The dynamic changes in the 2D shape of a droplet and the internal flows were measured by taking consecutive A-scans at a fixed x-position, while the Galvano mirror of the OCT system swept the beam across the droplet in the y-direction. 128 scans were taken along a sweep at a frequency of 36 kHz. This resulted in a step size of 6.25 μm, which ensures that the lateral resolution in the image was dictated by the optical resolution of 6.7 μm. At each y-position, a single 1D scan over the depth direction was made (and not 10000 consecutive scans as before), as this type of measurement does not aim at resolving the rapid temporal fluctuations inside the measurement volumes. The sequence of 128 1D scans across the droplet was used to construct a 2D scan (often referred to as a B-scan). Consecutive B-scans were taken at a frequency of 1 Hz during a drying period of 240 s. Hereafter, we colloquially refer to consecutive B-scans as '2D OCT' scans.

2.5. OCT signal processing - General

The raw interferometric OCT signals were acquired using ThorImage® software (Thorlabs Inc.) and post-processed with MATLAB (2017b). The processing consisted of the following steps. First, a reference spectrum was subtracted from the signal. Second, the resulting interference spectrum was interpolated in order to linearize the spectrum in wavenumber (because the raw interference spectrum depends on space on the spectrometer). The interpolation is essential to obtain bandwidth-limited axial resolution. Third, an inverse Fourier transform was applied to convert the signal from spectral to space-time domain (Izatt et al., 2015). Fourth, the absolute value was taken to obtain the final depth-resolved OCT amplitude $|a(i,j,k)|$, where the index i refers to the discretized spatial z-location along the depth of the droplets, j refers to the discretized y-location, and k to the discretized time. The index i covers 1024 pixels and spans 1.89 mm. The droplet occupied roughly 300 of these pixels in depth at the start of the drying experiment. A higher magnification was not possible as the axial range is determined by the spectrometer in the OCT system. The ranges for $j = 1 \ldots J$ and $k = 1 \ldots K$ depend on whether a fast 1D scan or a slower 2D scan was acquired, as detailed below.

2.6. OCT signal processing - Determination of the spatio-temporal diffusion coefficient of the TiO_2 particles

The first type of OCT measurement was done to resolve the spatio-temporal diffusion coefficient of the TiO_2 particles at a single and fixed lateral position ($J = 1$) along the droplet's center-line. A single sequence of 1D scans comprises $K = 10000$ consecutive scans, such that k runs from 1 to 10000. The temporal autocorrelation, $\alpha(i,j,k)$, was calculated for each sampling volume along the depth, i.e. for each i. Since there is a single y-position, we drop the index j and write

$$\alpha(i,l) = \begin{cases} \dfrac{1}{K-l}\sum_{k=1}^{K-l}\left(|a(i,k)| - \langle |a(i)| \rangle\right)\left(|a(i,k+l)| - \langle |a(i)| \rangle\right), & \text{if } l \geqslant 0 \\ \dfrac{1}{K-|l|}\sum_{k=1+|l|}^{K}\left(|a(i,k)| - \langle |a(i)| \rangle\right)\left(|a(i,k-|l|)| - \langle |a(i)| \rangle\right), & \text{if } l < 0 \end{cases}$$

with l the discretized lag index running from $-K+1$ to $K-1$ and $\langle |a(i)| \rangle$ the mean amplitude. The temporal autocorrelation for each sampling volume provides insights on the time scale of the fluctuations in scattering intensity indicative for the local diffusion coefficient of the TiO_2 particles, which depends on the local viscosity of the MD12 solution, and hence on the local MD12 concentration. The local diffusion coefficient was determined with two assumptions. First, assuming monodisperse particles, the decay of $\alpha(i,l)$ can be described by a single exponential decay. Second, assuming that particle diffusion causes the temporal decay, the field decorrelates at a rate of Dq^2, with diffusion coefficient D and the magnitude of the scattering vector q. This magnitude is calculated using $q = 4\pi n \sin(\theta/2)/\lambda$, with the scattering wavelength in vacuum λ, the refractive index of the medium n, and the scattering angle θ, which is 180° in OCT. We used the central wavelength $\lambda_c = 900$ nm as the scattering wavelength, as confirmed in previous work (Kalkman, Sprik, & van Leeuwen, 2010). Since we defined the OCT signal as the absolute value and the OCT magnitude is the product of two heterodyne intensities, the measured signal decorrelates at a rate of $2Dq^2$ (Kalkman et al., 2010). With these assumptions, the diffusion coefficient of the TiO_2 particles in each sampling volume, $D(i)$, can be determined by fitting $g(i,l) = A(i)e^{-2D(i)q^2 l/f}$ to $\alpha(i,l)$, with $A(i)$ an amplitude fitting parameter, $D(i)$ the fitted diffusion coefficient, and f the acquisition frequency of 5.5kHz. Fitting was done using nlinfit (MATLAB2017b). Only the data where α had not reached zero yet was used to fit $g(i,l)$. While the value of $A(i)$ at $l = 0$ equals 1 after normalization, we saw an immediate drop in amplitude due to shot noise and ignored $l = 0$ when fitting $A(i)$. We found that fits with $A(i)$ larger than 0.3 were accurate, i.e., with the initial decay visible above the noise levels. Fits with lower

values of $A(i)$ were excluded from further analysis. The depth-resolved diffusion coefficients obtained from the fits were converted from discretized positions to z-positions by multiplying i with the axial sampling resolution (1.95 μm) and accounting for the refractive index. The $D(z)$ along the center-line was determined for each 1D sequence, while the 1D sequences were taken at 0.27Hz to obtain the time-dependence. Hence, a spatio-temporal map of $D(z,t)$ was obtained. The influence of noise was reduced by applying a median filter (5×5) in space and time for the $D(z,t)$ map. The value of a data point was replaced with the median value of its neighbors in case its value deviated more than a factor 4 from the median value.

We conclude by pointing out that the acquisition range of $D(z,t)$ depends on the sampling frequency (5.5kHz) and the number of successive scans (10000) in a single sequence. The sampling frequency limits detection of short time scale fluctuations. We estimate, based on half of the decay occurring in the first ten scans, an upper limit of $D \approx$1.1E-12m^2 s^{-1}. For a given frequency, the number of scans in a sequence limits detection of longer time scale fluctuations. Assuming that half the decay occurs over 10000 scans, we estimate a lower limit of $D \approx$5.5E-16m^2 s^{-1} The settings used in the experiments were chosen based on the expected dynamic range of TiO_2 diffusion coefficients in the drying droplets.

2.7. Testing of the diffusion coefficient determination method

The accuracy of the diffusion coefficient determination method was tested using an aqueous 2.5 wt% solution of monodisperse polystyrene particles (Polysciences, Inc.) with a reported diameter of $d = 104 \pm 6$nm. This size was confirmed by measuring a diluted sample (0.26 wt%) with dynamic light scattering (Malvern Zetasizer Nano ZS), resulting in $d = 107 \pm 2$ nm. The accuracy test was done by dispensing several milliliters of the solution in a cuvette. The cuvette was sealed with a transparent cover to prevent evaporation and corresponding convective flows. The fitted $D(z)$ from 100 consecutive axial depths in the liquid was averaged and resulted in $\widehat{D} = 5 \pm 1$ μm^2 s^{-1}. The Stokes-Einstein equation was used to calculate the theoretical D of the polystyrene particles using the reported diameter as $D = 4.13 \pm 0.08$μm^2 s^{-1}. Hence, there was a good agreement between the D obtained with OCT and the theoretical D. The observed precision is acceptable for the purpose of the droplet drying measurements, because the diffusion coefficient in the droplet drying experiments is expected to change over several orders of magnitude. We repeated the cuvette measurements on two different occasions using the TiO_2 tracer particles in 10 wt% MD12 solution, resulting in $\widehat{D} = 0.4 \pm 0.2$ μm^2 s^{-1} and $\widehat{D} = 0.4 \pm 0.2$ μm^2 s^{-1}, showing a good reproducibility.

2.8. Determination of the spatio-temporal viscosity and concentration of the MD12 solution

The obtained diffusion coefficient $D(z,t)$ provides insights on the viscosity $\eta(z,t)$, and hence on the MD12 concentration $c(z,t)$. We used the Stokes-Einstein equation to determine the viscosity using $\eta(z,t) = k_BT/3\pi D(z,t)d$, with k_BT the thermal energy and d the diameter of the TiO_2 particles, which was determined before each experiment using the sealed cuvette method as described in the previous section. The MD12 concentration $c(z,t)$ was determined from Equation 5 in the work by Both et al. (2019) on aqueous MD12 solutions. We used the fitting parameters found by the authors for calculating $c(z,t)$ from $\eta(z,t)$. Since our work used the same maltodextrin batches as the work of Both et al. (2019), we can use their fitted parameters for this calculation without introducing errors due to batch differences.

2.9. OCT signal processing - Droplet drying kinetics and internal flow

The 2D OCT measurements were done to (i) determine the dynamic changes in the 2D shape of the droplets, (ii) detect the formation of a concentrated skin, and (iii) capture the internal flows. Unlike the 1D scan, the 2D scan does not comprise temporal information ($K = 1$), but it does comprise 1D scans at 128 y-positions ($J = 128$). Hence, a single sequence $|a(i,j,k=1)|$ shows the (quasi-) instantaneous amplitude in the 2D cross section of the droplet. This sequence is repeated at 1 Hz to capture the dynamic changes during the drying period of 240 s.

The 2D shape of the droplets and the substrate location can be obtained from the OCT intensity. A circle fitting algorithm was used to fit a circle to the detected droplet interface for calculating the height $h(t)$ and the radius $R(t)$ of the droplet as a function of time. From these parameters, the equivalent spherical diameter $d(t)$ was calculated using the geometrical relation for a spherical cap. Since we observed that the hollow particle that formed has the shape of a spherical cap, we used the spherical-cap description throughout the drying process.

The internal flow inside the droplet was determined by analyzing subsequent 2D OCT images using a particle image velocimetry algorithm implemented in DaVis software (LaVision, Germany). The onset of skin formation and the thickness of this skin were analyzed using the variance in intensity, further explained in the results section.

3. Results and discussion

3.1. Drying kinetics from 2D OCT images

Before we discuss the kinetics of the droplet drying process, we first discuss the general features visible in the 2D OCT images of a drying droplet. The first panel in Fig. 2a shows the 2D cross section of a sessile droplet shortly after the start of the drying experiment. The droplet is visible as a bright speckled area arising from the scattering of light from tracers against a dark background of the surrounding air where no backscattering takes place. The surface of the flat substrate is visible as the bright horizontal line from specularly reflected light, extending left and right from the droplet, which is best visible in the other three panels where the droplet has shrunk. The panels show that the droplet appears to extend into the flat substrate. While a similar observation is seen in brightfield microscopy images taken from the side of sessile droplets (Both et al., 2018), the explanation for this observation is different. In brightfield images, it is a reflection that itself does not contain information. In the OCT images, extension into the substrate is caused by a difference between the length of the path traveled through the air (physical path) and through the liquid droplet (optical path). We note that the substrate, which appears curved beneath the droplet, is hardly visible due to substantial multiple scattering. For the construction of the 2D OCT images, we used the physical path length, with a spacing between pixels in the z-direction of 1.84 μm. The optical path length is a factor 1.33 longer, which stems from the ratio of the refractive indices of liquid and air. The flat substrate is displayed at the correct height outside the droplet, but it appears lower inside the droplet due to the longer optical path (Manukyan et al., 2013; Edwards et al., 2018). The air-liquid interface is displayed at the correct location. Hence, we can use the 2D OCT images to analyze how the shape of the droplet evolves in time. Only close to the substrate, the interface cannot be resolved for droplets at hydrophobic substrates (contact angle over 90°), as the beam is strongly deflected at the edges of the droplet (Manukyan et al., 2013).

Besides the external shape of the droplet, OCT images have the great advantage of also showing the internal structures of the droplet. The fourth panel, measured at 250 s, shows a dark area inside the droplet that has the same brightness as the background. The absence of scattering particles and what looks like the substrate being slightly visible at approximately the same height as outside the droplet, indicates that a gaseous vacuole has formed. The morphology of the fully dried droplet under the used conditions is a hollow spherical cap. Since the final morphology depends on the redistribution of solute and hence on the drying conditions, other morphologies have also been reported in literature for MD12 solutions (Both et al., 2018; Bylaitë, Venskutonis, & Mapdpierienë, 2001; Siemons et al., 2020).

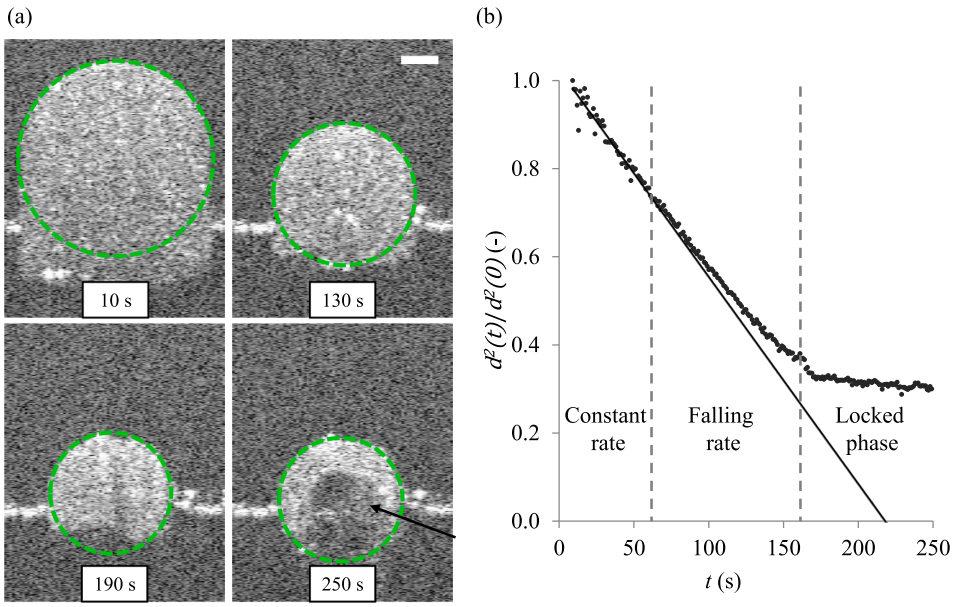

Fig. 2. Drying kinetics. (a) Selected images from the 2D OCT-scans at 10 s, 130 s, 190 s and 250 s of evaporation. Brighter pixels correspond to greater scattering intensity. The scale-bar is 100 μm. The green circles indicate the fitting result. The black arrow indicates the vacuole. (b) Droplet drying kinetics from the application of the circle fitting algorithm to the 2D scans. With d being the equivalent spherical diameter. The two dashed lines indicate the regime transitions as analyzed from the drying curve. A linear trendline is fitted through the initial 20 s for comparison of the measured drying curve with the constant drying rate curve. (For interpretation of the references to colour in this figure legend, the reader is referred to the web version of this article.)

We quantified the drying kinetics of the droplet by analyzing the dynamic change in the external shape of the droplet, see supplementary video 1 for a video of the 2D OCT images. The theory for drying droplets without solute predicts that the diameter of a spherical droplet decreases with the square root of time (Jakubczyk, Kolwas, Derkachov, Kolwas, & Zientara, 2012). Hence, we expect the square of the droplet diameter to linearly decrease in time until the accumulation of MD12 at the air-liquid interface starts to hinder the evaporation process. We fitted a circle to the shape of the droplet in each of the consecutive 2D OCT images using the routine explained before and plotted the normalized square of the diameter ($d^2(t)/d^2(0)$) as a function of time. Initially, the d^2 indeed decreased linearly in time, which is seen in Fig. 2b. The initial drying rate, κ, found by fitting the measured d^2 in the first 20 s against the relation $d^2 = d_0^2 - \kappa t$ with $d_0 = 432$ μm, is equal to $\kappa = 8.8\text{E}2$ μm^2 s^{-1}. Based on this initial rate, full evaporation of the droplet is expected to take 213 s. After the first regime with drying at a constant rate, a second

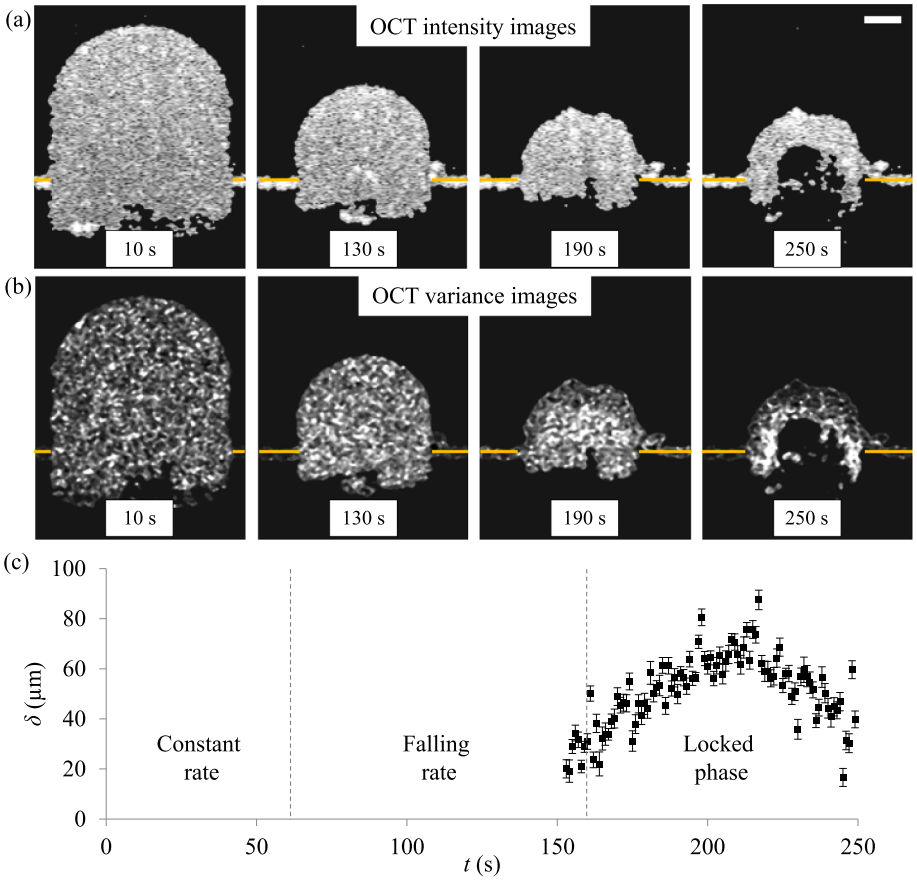

Fig. 3. Convective flow characterization. The scale-bar is 100 μm. (a) Velocity vector field at $t = 9$ s, as obtained from the particle image velocimetry analysis. Blue indicates a low velocity and orange indicates a high velocity. The yellow box indicates the region from which the mean upward velocity $\hat{u}$ was determined. (b) Mean upward velocity $\hat{u}$ during droplet drying. The gray bars show the standard deviation. (For interpretation of the references to colour in this figure legend, the reader is referred to the web version of this article.)

regime is visible in which drying occurs at a decreasing rate. The transition between the two regimes occurs around 60 s, observed as a deviation of the data from the linear fit, see Fig. 2b. After about 160 s, a third regime is visible, referred to as the locking phase, in which the shape remains constant indicative for reaching a critical surface concentration (Mezhericher et al., 2012). At the transition between the second and third regime, known as the locking point, invagination of the droplet surface starts near the droplet's apex, eventually forming a vacuole inside the droplet. Surface invagination close to the apex has been reported in previous work and can be attributed to inhomogeneous evaporation (Bouman, Venema, de Vries, van der Linden, & Schutyser, 2016; Bansal et al., 2015). The onset of the invagination can be seen in the third panel (190 s) of Fig. 2a as a concave deformation of the interface. With OCT, it is easily confirmed that the forming vacuole contains gas, as the extension effect due to a difference in refractive index is suppressed in the region of the vacuole, there is no observable scattering and the location of the planar substrate is at the same height as the location of the substrate outside the droplet (Fig. 2a - 250 s). While OCT, like brightfield imaging, allows determining the drying curve, including the transitions between the three regimes, it also allows studying the formation of the skin and determining the spatio-temporal viscosity and MD12 concentration, as detailed later.

3.2. Internal flow from 2D OCT images

The 2D OCT images can also be used to get an impression of the internal flow, with the TiO_2 agglomerates acting as tracer particles. The scattering of the individual agglomerates was sufficient to allow performing particle image velocimetry on the 2D OCT images. Hence, we analyzed the 2D OCT images to get an estimation of the magnitude of the internal flow along the center-line of the droplet. This information is essential to confidently quantify the contribution of convection when later analyzing the fast 1D OCT scans to resolve the spatio-temporal diffusion coefficient of the TiO_2 particles, as well as the viscosity and the MD12 concentration along the center-line of the droplet.

A recirculation flow pattern was observed in the droplet, with an upward flow in the center and a downward flow along the interface, see Fig. 3a. Other work has shown that this pattern is characteristic for droplets on hydrophobic substrates and caused by inhomogeneous evaporation that results in thermocapillary driven flows, also known as Marangoni flows (Manukyan et al., 2013; Edwards et al., 2018) The largest velocities were found in the central region, which is where the 1D OCT scans were performed. The average velocity $\hat{u}$ in the central region indicated by the yellow rectangle is about 20 μm s^{-1} at the start of drying, see Fig. 3b. This velocity gradually decreases, which is explained by the increasing viscosity of the droplet as evaporation proceeds.

3.3. Skin formation from 2D OCT images

The 2D OCT images were also used to study the formation of a solid skin at the droplets interface. The temporal fluctuations in brightness in subsequent 2D images contain information about the dynamics. Rapid fluctuations correspond to liquid regions, while slower fluctuations correspond to highly viscous or solid regions. We started the analysis by removing the background of the raw 2D OCT images presented in Fig. 2a, see the result in Fig. 4a. We then analyzed the temporal variation in the intensity of each pixel for a moving time window of 3 subsequent images, which we found to be optimal for identifying skin and bulk after testing a range of 2–11 subsequent images. The values of the variance σ^2 are presented in the panels in Fig. 4b, with a higher brightness corresponding to a higher variance. In the first two panels, the brightness is uniform across the droplet. The last two panels show a darkened area near the interface with less fluctuations that is indicative of a solidifying skin.

We quantified the dynamics of skin formation as follows: for each image, we determined the center of the circle that describes the interface. Then, while ignoring all pixels below that center, we analyzed the variance as a function of the distance from the center $\sigma^2(r)$. The transition from liquid to solid is gradual, which results in a gradual decrease of $\sigma^2(r)$ with increasing r. We fitted the profile $\sigma^2(r)$ with an arbitrary exponential function $p(r) = \sigma^2_{min} + (\sigma^2_{max} - \sigma^2_{min}) \cdot e^{(-1.2^{r-b})}$ with σ^2_{min} and σ^2_{max} the minimum and maximum variance along the radius, respectively. The factor 1.2 in the exponent was manually determined to match the curve of $p(r)$ with the gradual decrease of the variance at the transition point. The location r_{skin} along the line where the variance was halfway its minimum and maximum value, i.e. $e^{(-1.2^{r_{skin}-b})} = 0.5$, was taken as the transition between solid and liquid. For each image, we determined the skin thickness, $\delta = R - r_{skin}$, with $R(t)$ the fitted droplet radius. By analyzing consecutive images, we determined how the skin thickness increases in time $\delta(t)$. We divided the obtained thickness by the refractive index of water to correct for the optical extension in the OCT images.

Fig. 4c show the dynamics of the skin thickness $\delta(t)$. Skin formation starts about 15 s before locking of the droplet. At the start of the third regime, the skin grew to a thickness of 20 ± 3 μm. The skin reaches a maximum of 87 ± 2 μm at 217 s. Interestingly, $\delta(t)$ decreases to about 40 μm as the end of drying approaches. From supplementary video 2, which shows the variance images, this effect looks to be caused by the moving front of the vacuole, which appears to compress the stagnant skin region. Comparing the measured skin thickness to the thickness estimated based on the total solids content provides a clue about how dry the stagnant layer is. With an initial droplet volume of 4.2E-11 m^3 and an initial

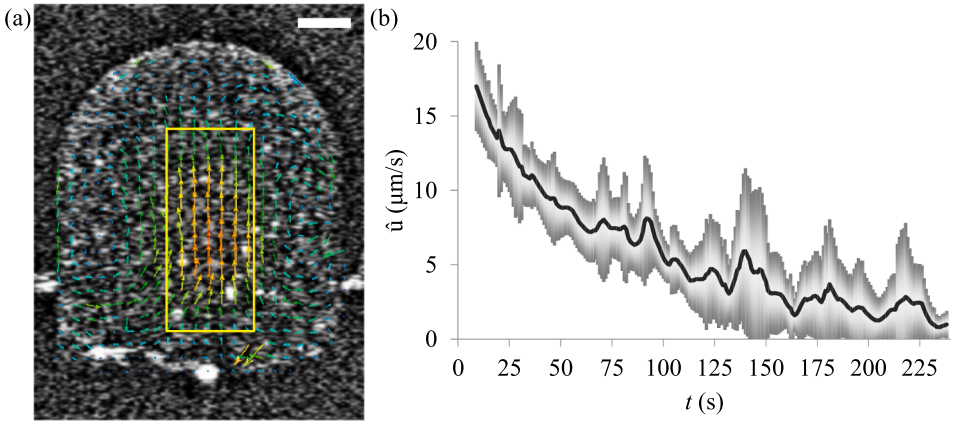

Fig. 4. Detection of the stagnant skin from the 2D OCT scans. The scale-bar is 100 μm. (a) OCT 2D intensity images with the droplet isolated from the background. (b) The images constructed from the temporal variance of the OCT intensity. (c) The skin thickness $\delta(t)$ as determined from the variance figures in (b). The error bars indicate the 95% confidence interval of the fit. The regimes, as found in Fig. 2, are also indicated in the figure.

concentration of 10 wt%, the total solids contents is 5.1 μg. Assuming the skin to be fully dry and amorphous, the volume of the skin follows from the total solids contents and the density of dry amorphous maltrodextrin (1.1–1.4 gm L^{-1} (Takeiti, Kieckbusch, & Collares-Queiroz, 2010)). With an outer radius of 141 μm at 250 s, we estimate the thickness of the skin to be about 20 μm. The measured skin thickness is about 40 μm, showing that the stagnant layer observed in the measurements is not fully dry.

3.4. Measuring the dynamic intra-droplet solute redistribution

3.4.1. Spatio-temporal diffusion coefficient of TiO_2 particles

We now turn to the main point of the paper, which is to explore the use of OCT to determine the spatio-temporal redistribution of solute in a drying droplet. This redistribution of solute was measured using the fast 1D OCT data obtained along the center-line of the droplet. A map of the diffusion coefficient, $D(z,t)$, is shown in Fig. 5a. Initially, the diffusion coefficient is uniform across the height of the droplet, which is consistent with a uniform distribution of TiO_2, and averages to $D = 2.9\text{E-}13 m^2 s^{-1}$. Over time, the diffusion coefficient in the region near the interface decreases, seen from the change from yellow to purple. Additionally, the region at the interface with a reduced diffusion coefficient widens over time. Further inspection of the autocorrelation curves in the low D region near the interface showed that the lowest measurable diffusion coefficient was $D \approx 5.3\text{E-}15\ m^2\ s^{-1}$, which is larger than the estimated lower detection limit of $D \approx 5.5\text{E-}16\ m^2\ s^{-1}$. For values of D below the measurable ones, the amplitude of the autocorrelation function was too low ($A < 0.3$) to perform a faithful fit. The reason for why the estimated lower detection limit was not reached is not clear, although, we expect that over the timescale of the entire M-scan accumulation of noise leads to a reduced signal quality. When reaching $t = 195$s, the measured height becomes zero, and only the bright line of the PDMS substrate remained on the OCT scan. Visual observation post factum showed that a vacuole had formed inside the droplet, similar to what was seen in Fig. 2a, but, the hole in the shell that lead to the vacuole formed at the droplet's apex. Hence, the OCT bundle went through the hole hitting the PDMS substrate without hitting parts of the partially-dried droplet. We can identify this time where the measured height goes to zero as the transition to the third drying regime. Since we had no access to the spherical diameter of this droplet, the transition to the second regime was not determined.

A final feature we point out in the map is the growing region of decreasing diffusion coefficient near the substrate. The diffusion coefficient in this region differs at least one order of magnitude from the diffusion coefficient in the core of the droplet. Fig. 5a shows that this region grows to a thickness of about 10μm in the first 100s. The decreased diffusion coefficient indicates that MD12 accumulates near the substrate, which may be attributed to the internal recirculations (Bansal et al., 2015; Bansal, Sanyal, Kabi, Pathak, & Basu, 2018) as observed in the particle image velocimetry analysis of the 2D OCT scans.

3.4.2. Contribution of convective flow to measurement of $D(z,t)$

The autocorrelation of the 1D OCT scans used to determine the spatio-temporal diffusion coefficient of the TiO_2 particles is affected by diffusion and convection of those particles. We neglected the convective contribution in our quantitative analysis. Here, we justify that. The contribution to the autocorrelation of the 1D OCT scans by convective flow is described by $e^{-2\left[\frac{u_z l}{w_z f}\right]^2}$, with l the discretized lag time, f the acquisition frequency, u_z the velocity in the direction of the beam, and w_z the beam radius in the axial direction. For Fourier-domain OCT, the axial beam radius is approximately equal to the coherence length of 2.6μm (Weiss, van Leeuwen, & Kalkman, 2015). The contribution by diffusion is described by $e^{-2Dq^2 l/f}$. The two contributions are multiplicative in the autocorrelation function, such that the contribution by convection can be neglected with respect to the contribution by diffusion when $[(fw_z^2)/(lu_z^2)]/(Dq^2)^{-1} \gg 1$. Using the values for u_z and D at the start of drying, i.e. $v_z \approx 20\mu m\ s^{-1}$ and $D \approx 3\text{E-}13 m^2\ s^{-1}$, together with a lag time of $l/f = 18/5500$ s as estimated from $e^{-2Dq^2 l/f} \approx 0.5$, we find that this criterion is met by two orders of magnitude. During drying, the convective flow velocity lessens in the bulk region and becomes negligible in the skin region. Considering a drying time of $t \approx 140$ s, at which we take a conservative velocity of $u_z = 10\ \mu m\ s^{-1}$, a diffusion coefficient in the bulk region of $D \approx 6\text{E-}14 m^2\ s^{-1}$, and a lag time of $l/f = 93/5500$ s for $e^{-2Dq^2 l/f} \approx 0.5$, we find, again, that the criterion is met by two orders of magnitude. While we considered the axial velocity in this analysis, the lateral velocity also influences the correlation, however, it is significantly lower than the axial velocity as evident from Fig. 3 and its contribution can be safely neglected. Hence, the contribution of both axial and lateral convection to the decay of the autocorrelation function can be confidently neglected under the here-tested conditions.

3.4.3. Spatio-temporal viscosity and concentration of MD12 solution

We determined the spatio-temporal viscosity $\eta(z,t)$ and, subse-

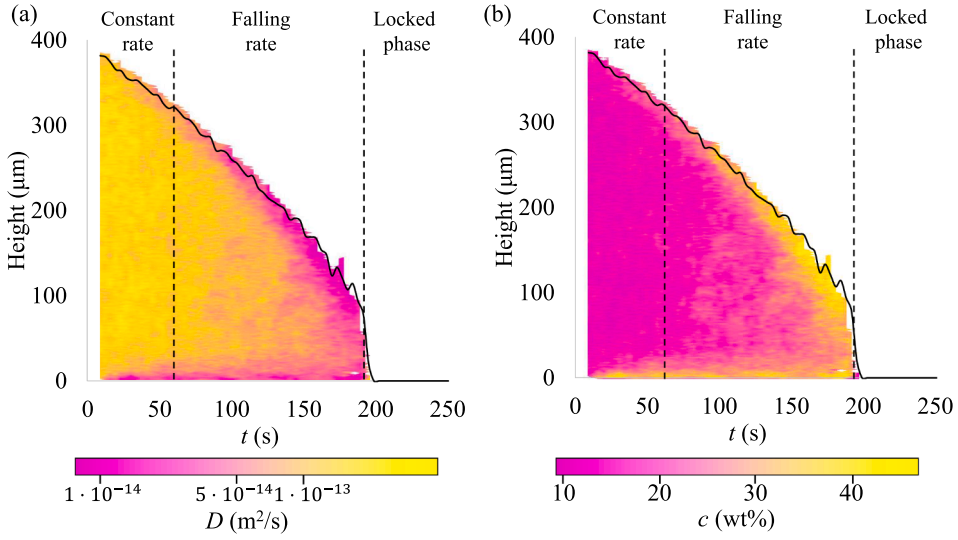

Fig. 5. Mapping of the intra-droplet properties. (a) Local logarithmic diffusion coefficient of the TiO_2 particles. (b) Local MD12 concentration. In both figures, the black line indicates the height of the droplet, as determines from the 1D OCT scans. The dashed lines indicate the transition between the different drying regimes.

quently, the MD12 concentration $c(z,t)$ based on the spatio-temporal diffusion coefficient of the TiO_2 particles as explained in Section 2.8. The features in the MD12 concentration map are similar to the features in the map of the diffusion coefficient of the TiO_2 particles. The concentration map is shown in Fig. 5b. The initial concentration averaged over the depth of the droplet is 14 ± 2wt%, slightly larger than the 10 wt % of the prepared MD12 solution, partly explained by the first OCT scan being taken about 10s after dispensing the droplet. Another explanation is the lower accuracy for the concentration measurement at lower concentrations, as the $\eta(c)$ curve remains comparatively flat for low concentrations (<30 wt%) and strongly increases for higher concentrations (Both et al., 2019). Hence, a relatively small measurement error would have a greater effect on the resulting concentration at lower concentrations. At $t = 60$ s, which is when the droplet in the 2D OCT scan transitioned to the second drying regime, the bulk concentration was 15 ± 2 wt%, while the concentration near the air-liquid interface increased to 23 ± 3 wt%. From then onward, the concentration near the interface further increased to the maximum measurable concentration of 46 wt%. Around the transition to the third drying regime, the bulk concentration had also noticeably increased to values over >30wt%. Based on this it is unclear whether the transition to the third drying regime is due to reaching a critical surface concentration ($\approx$ 46 wt%), or, because the bulk concentration became elevated.

It is worthwhile to compare the measured $c(z,t)$ map to typical results from numerical approaches that determine the spatio-temporal concentration of solute in an evaporating droplet. Numerical approaches commonly show an exponential shape of the radial solute concentration, where the surface layer has a highly elevated concentration compared to the center of the droplet. This exponential shape is maintained until the surface layer reaches a critical condition, which is, typically, when the surface layer solidifies (Porowska et al., 2016). The measured $c(z,t)$ map also shows a sharp increase of concentration from the bulk to the interface, but from about 100 s onward, the concentration appears to plateau at concentrations between 40 wt% and 46 wt%. However, the viscosity at $c \approx$46 wt% is only $\eta \approx$0.1 Pa s, while viscosity measurements have shown that MD12 remains liquid-like up to concentrations of $\approx$ 70 wt% (Both et al., 2019). Hence, we expect the concentration to exceed the highest measurable value of 46 wt%. While further experimental research is needed to resolve the higher concentrations at the interface, we do demonstrate that OCT can quantitatively measure the concentration of solutes dynamically in time inside a drying droplet.

The use of OCT for other materials, especially those with increased complexity such as milk powders, is of interest. In this work, we used a binary system (maltodextrin in water) for which the relation between the viscosity and maltodextrin concentration is known, making it possible to determine the spatio-temporal maltodextrin concentration from the spatio-temporal viscosity. This is also possible for multi-component systems for which a combination of concentrations of the various components uniquely relates to the viscosity of the mixture. Care should be taken when dealing with multi-component mixtures in which components unmix during evaporation (Both et al., 2018). While it may be difficult to determine the individual spatio-temporal concentrations in such systems, the spatio-temporal viscosity can be measured and used for optimization or validation purposes.

4. Conclusion

The goal of this work was to explore the use of optical coherence tomography to study drying of turbid solute-containing droplets, with the emphasis on measuring the dynamic redistribution of solute during drying. Using aqueous droplets containing maltodextrin as a model system, we demonstrated that OCT can be used to measure the drying kinetics, the internal flows, and the development of internal structures inside drying droplets, such as the solidifying skin on the air-liquid interface and the growth of a gaseous vacuole. Moreover, we demonstrated that spatio-temporal maltodextrin concentration maps can be obtained over the center-line of a sessile droplet, providing an advantage over conventional single droplet drying methods. We think that the ability to measure the dynamic redistribution of solutes and linking it to the development of the morphology of dried particles is instrumental for the rational design of powders with specific properties and for the optimization of process equipment such as spray dryers. Additionally, we think that the ability to measure the spatio-temporal concentrations is important for the validation of numerical models that aim to predict the morphology or drying droplets and their agglomeration behavior from the development of spatio-temporal concentrations during drying. While the here presented experimental method focuses on sessile droplets that are larger than droplets typically encountered in spray dryers, we think that mechanistic insights obtained from a quantitative comparison between experiments and numerical models at the scale of sessile droplets guides our mechanistic understanding of drying of smaller droplets relevant for spray drying processes.

Declaration of Competing Interest

The authors declare that they have no known competing financial interests or personal relationships that could have appeared to influence the work reported in this paper.

Acknowledgements

This scientific work is supported by the Netherlands Organization for Scientific Research (NWO) (Grant No. 15459).

Appendix A. Supplementary material

Supplementary data associated with this article can be found, in the online version, at https://doi.org/10.1016/j.foodres.2022.111049.

References

Bansal, L., Miglani, A., & Basu, S. (2015). Universal buckling kinetics in drying nanoparticleladen droplets on a hydrophobic substrate. *Physical Review E, 92*(4), Article 042304. https://doi.org/10.1103/physreve.92.042304

Bansal, L., Sanyal, A., Kabi, P., Pathak, B., & Basu, S. (2018). Engineering interfacial processes at mini-micro-nano scales using sessile droplet architecture. *Langmuir, 34* (29), 8423–8442. https://doi.org/10.1021/acs.langmuir.7b04295

Both, E. M., Nuzzo, M., Millqvist-Fureby, A., Boom, R. M., & Schutyser, M. A. I. (2018). Morphology development during single droplet drying of mixed component formulations and milk. *Food Research International, 109*, 448–454. https://doi.org/10.1016/j.foodres.2018.04.043

Both, E. M., Siemons, I., Boom, R. M., & Schutyser, M. A. I. (2019). The role of viscosity in morphology development during single droplet drying. *Food Hydrocolloids, 94*, 510–518. https://doi.org/10.1016/j.foodhyd.2019.03.023

Bouman, J., Venema, P., de Vries, R. J., van der Linden, E., & Schutyser, M. A. I. (2016). Hole and vacuole formation during drying of sessile whey protein droplets. *Food Research International, 84*, 128–135. https://doi.org/10.1016/j.foodres.2016.03.027

Bylaitë, E., Venskutonis, P. R., & Mapdpierienë, R. (2001). Properties of caraway (carum carvi l.) essential oil encapsulated into milk protein-based matrices. *European Food Research and Technology, 212*(6), 661–670. https://doi.org/10.1007/s002170100297

Callewaert, T., Dik, J., & Kalkman, J. (2017). Segmentation of thin corrugated layers in high-resolution OCT images. *Optics Express, 25*(26), 32816–32828. https://doi.org/10.1364/oe.25.032816

Davidson, Z. S., Huang, Y., Gross, A., Martinez, A., Still, T., Zhou, C., Collings, P. J., Kamien, R. D., & Yodh, A. G. (2017). Deposition and drying dynamics of liquid crystal droplets. *Nature Communications, 8*(1), 1–7. https://doi.org/10.1038/ncomms15642

De Souza Lima, R., Ré, M.-I., & Arlabosse, P. (2020). Drying droplet as a template for solid formation: A review. *Powder Technology, 359*, 161–171. https://doi.org/10.1016/j.powtec.2019.09.052

Edwards, A. M. J., Atkinson, P. S., Cheung, C. S., Liang, H., Fairhurst, D. J., & Ouali, F. F. (2018). Density-driven flows in evaporating binary liquid droplets. *Physical Review Letters, 121*(18), Article 184501. https://doi.org/10.1103/physrevlett.121.184501

Foerster, M., Gengenbach, T., Woo, M. W., & Selomulya, C. (2016). The influence of the chemical surface composition on the drying process of milk droplets. *Advanced Powder Technology, 27*(6), 2324–2334. https://doi.org/10.1016/j.apt.2016.07.004

Fu, N., Woo, M. W., & Chen, X. D. (2012). Single droplet drying technique to study drying kinetics measurement and particle functionality: A review. *Drying Technology, 30* (15), 1771–1785. https://doi.org/10.1080/07373937.2012.708002

Griffith, J. D., Bayly, A. E., & Johns, M. L. (2008). Magnetic resonance studies of detergent drop drying. *Chemical Engineering Science, 63*(13), 3449–3456. https://doi.org/10.1016/j.ces.2008.03.043

Izatt, J. A., Choma, M. A., & Dhalla, A.-H. (2015). *Optical Coherence Tomography*. Berlin, Heidelberg: Springer. https://doi.org/https://doi.org/10.1007/978-3-540-77550-8_2.

Jakubczyk, D., Kolwas, M., Derkachov, G., Kolwas, K., & Zientara, M. (2012). Evaporation of micro-droplets: The 'radius-square-law' revisited. *Acta Physica Polonica-Series A General Physics, 122*(4), 709. https://doi.org/10.12693/aphyspola.122.709.

Kalkman, J., Sprik, R., & van Leeuwen, T. G. (2010). Path-length-resolved diffusive particle dynamics in spectral-domain optical coherence tomography. *Physical Review Letters, 105*(19), Article 198302. https://doi.org/10.1103/physrevlett.105.198302

Koponen, A. I., & Haavisto, S. (2020). Analysis of industry-related flows by optical coherence tomography–a review. *KONA Powder and Particle Journal, 2020003*. https://doi.org/10.14356/kona.2020003.

Lee, J., Bathany, C., Ahn, Y., Takayama, S., & Jung, W. (2016). Volumetric monitoring of aqueous two phase system droplets using time-lapse optical coherence tomography. *Laser Physics Letters, 13*(2), Article 025606. https://doi.org/10.1088/1612-2011/13/2/025606

Lemoine, F., & Castanet, G. (2013). Temperature and chemical composition of droplets by optical measurement techniques: A state-of-the-art review. *Experiments in Fluids, 54*(7), 1–34. https://doi.org/10.1007/s00348-013-1572-9

Manukyan, S., Sauer, H. M., Roisman, I. V., Baldwin, K. A., Fairhurst, D. J., Liang, H., Venzmer, J., & Tropea, C. (2013). Imaging internal flows in a drying sessile polymer dispersion drop using spectral radar optical coherence tomography (sroct). *Journal of Colloid and Interface Science, 395*, 287–293. https://doi.org/10.1016/j.jcis.2012.11.037

Meerdink, G., & van't Riet, K. (1995). Modeling segregation of solute material during drying of liquid foods. *AIChE Journal, 41*(3), 732–736. https://doi.org/10.1002/aic.690410331

Mezhericher, M., Levy, A., & Borde, I. J. D. T. (2010). Theoretical models of single droplet drying kinetics: A review. *Drying Technology, 28*(2), 278–293. https://doi.org/10.1080/07373930903530337

Mezhericher, M., Naumann, M., Peglow, M., Levy, A., Tsotsas, E., & Borde, I. (2012). Continuous species transport and population balance models for first drying stage of nanosuspension droplets. *Chemical Engineering Journal, 210*, 120–135. https://doi.org/10.1016/j.cej.2012.08.038

Munoz-Ibanez, M., Nuzzo, M., Turchiuli, C., Bergenståhl, B., Dumoulin, E., & Millqvist-Fureby, A. (2016). The microstructure and component distribution in spray-dried emulsion particles. *Food Structure, 8*, 16–24. https://doi.org/10.1016/j.foostr.2016.05.001

Nuzzo, M., Overgaard, J. S., Bergenståhl, B., & Millqvist-Fureby, A. (2017). The morphology and internal composition of dried particles from whole milk–from single droplet to full scale drying. *Food Structure, 13*, 35–44. https://doi.org/10.1016/j.foostr.2017.02.001

Nuzzo, M., Sloth, J., Brandner, B., Bergenstahl, B., & Millqvist-Fureby, A. (2015). Confocal raman microscopy for mapping phase segregation in individually dried particles composed of lactose and macromolecules. *Colloids and Surfaces A: Physicochemical and Engineering Aspects, 481*, 229–236. https://doi.org/10.1016/j.colsurfa.2015.04.044

Porowska, A., Dosta, M., Fries, L., Gianfrancesco, A., Heinrich, S., & Palzer, S. (2016). Predicting the surface composition of a spray-dried particle by modelling component reorganization in a drying droplet. *Chemical Engineering Research and Design, 110*, 131–140. https://doi.org/10.1016/j.cherd.2016.03.007

Quiño, J., Hellwig, T., Griesing, M., Pauer, W., Moritz, H.-U., Will, S., & Braeuer, A. (2015). One-dimensional raman spectroscopy and shadowgraphy for the analysis of the evaporation behavior of acetone/water drops. *International Journal of Heat and Mass Transfer, 89*, 406–413. https://doi.org/10.1016/j.ijheatmasstransfer.2015.05.053

Sadek, C., Schuck, P., Fallourd, Y., Pradeau, N., Le Floch-Fouéré, C., & Jeantet, R. (2015). Drying of a single droplet to investigate process–structure–function relationships: a review. *Dairy Science and Technology, 95*(6), 771–794. https://doi.org/10.1007/s13594-014-0186-1

Santos, D., Maurício, A.C., Sencadas, V., Santos, J.D., Fernandes, M.H., & Gomes, P.S. (2018). Spray drying: An overview (R. Pignatello, Ed.). IntechOpen. UK. doi: 10.5772/intechopen.72247.

Schutyser, M. A. I., Both, E. M., Siemons, I., Vaessen, E. M. J., & Zhang, L. (2019). Gaining insight on spray drying behavior of foods via single droplet drying analyses. *Drying Technology, 37*(5), 525–534. https://doi.org/10.1080/07373937.2018.1482908

Sewalt, E. J. G., Zhang, F., van Steijn, V., van Ommen, J. R., & Meesters, G. M. H. (2020). Static and dynamic stickiness tests to measure particle stickiness. *KONA Powder and Particle Journal, 2021017*. https://doi.org/10.14356/kona.2021017.

Siemons, I., Politiek, R. G. A., Boom, R. M., van der Sman, R. G. M., & Schutyser, M. A. I. (2020). Dextrose equivalence of maltodextrins determines particle morphology development during single sessile droplet drying. *Food Research International, 131*, Article 108988. https://doi.org/10.1016/j.foodres.2020.108988

Srinivasan, V., Pamula, V. K., Rao, K. D., Pollack, M. G., Izatt, J. A., & Fair, R. B. (2003). *3-d imaging of moving droplets for microfluidics using optical coherence tomography*. California USA, Citeseer: Squaw Valley. https://doi.org/10.1.1.575.7151.

Takeiti, C. Y., Kieckbusch, T. G., & Collares-Queiroz, F. P. (2010). Morphological and physicochemical characterization of commercial maltodextrins with different degrees of dextrose-equivalent. *International Journal of Food Properties, 13*(2), 411–425. https://doi.org/10.1080/10942910802181024

Tuckermann, R., Puskar, L., Zavabeti, M., Sekine, R., & McNaughton, D. (2009). Chemical analysis of acoustically levitated drops by raman spectroscopy. *Analytical and Bioanalytical Chemistry, 394*(5), 1433–1441. https://doi.org/10.1007/s00216-009-2800-2

Van Der Kooij, H. M., Fokkink, R., Van Der Gucht, J., & Sprakel, J. (2016). Quantitative imaging of heterogeneous dynamics in drying and aging paints. *Scientific Reports, 6* (1), 1–10. https://doi.org/10.1038/srep34383

van der Hoeven, M. (2008). In *Particle-droplet collisions in spray drying (Ph.D Thesis). School of Engineering*. The University of Queensland.

Vehring, R., Foss, W. R., & Lechuga-Ballesteros, D. (2007). Particle formation in spray drying. *Journal of Aerosol Science, 38*(7), 728–746. https://doi.org/10.1016/j.jaerosci.2007.04.005

Walton, D. E. (2000). The morphology of spray-dried particles a qualitative view. *Drying Technology, 18*(9), 1943–1986. https://doi.org/10.1080/07373930008917822

Weiss, N., van Leeuwen, T. G., & Kalkman, J. (2015). Simultaneous and localized measurement of diffusion and flow using optical coherence tomography. *Optics Express, 23*(3), 3448–3459. https://doi.org/10.1364/oe.23.003448